

Nonlinear dynamics of traveling waves in rotating Rayleigh-Bénard convection: Effects of the boundary conditions and of the topology

Emmanuel Plaut

LEMTA, INPL-UHP-CNRS, 2 Avenue de la Forêt de Haye, F-54504 Vandœuvre Cedex, France

(Received 13 November 2002; published 15 April 2003)

Motivated by the experimental results of Liu and Ecke (1997, 1999), different models are developed to analyze the weakly nonlinear dynamics of the traveling-wave sidewall modes appearing in rotating Rayleigh-Bénard convection. These models assume fully rigid boundary conditions for the velocity field. At the linear level, this influences most strongly the critical frequencies: they appear to be proportional to the logarithm of the Coriolis number, which is twice the inverse of the Ekman number. An annular flow domain is considered. This multiply connected geometry is shown to lead generally to the existence of a *global* mean-flow mode proportional to the average, over the azimuthal coordinate, of the square of the modulus of the envelope of the waves. Because this mode feeds back on the active wave modes at cubic order, the resulting Ginzburg-Landau envelope equation contains a *nonlocal* term. This new term, however, vanishes in the large-gap limit relevant to the experiments of Liu and Ecke. As compared with previous theoretical work, the present models lead to reduced discrepancies with the results of these experiments concerning the coefficients of the envelope equation. It is also shown that the new nonlocal effects may be realized experimentally in a small-gap annular geometry if a small-Prandtl-number fluid is used, despite the fact that no regime of Benjamin-Feir instability is predicted to occur.

DOI: 10.1103/PhysRevE.67.046303

PACS number(s): 47.20.Ky, 47.20.Bp, 47.35.+i

I. INTRODUCTION

Nonlinear waves are ubiquitous in nature: they appear in biological, chemical, mechanical or optical systems, where they often play a crucial role. The simplest and most universal model capable of describing some relevant features of their nonlinear dynamics is the Ginzburg-Landau envelope equation

$$\begin{aligned} \tau(\partial_t A + v_g \partial_x A) = (1 + ic_0)\epsilon A + \xi^2(1 + ic_1)\partial_x^2 A \\ - \gamma(1 + ic)|A|^2 A \end{aligned} \quad (1)$$

for a quasiunidimensional system extended in the x direction. This equation for the slowly varying envelope $A = A(x, t)$ of the waves can be shown to hold rigorously when $\epsilon \rightarrow 0$ in the case of a supercritical instability, ϵ being the reduced distance to the onset of the instability [1]. The dynamical features described by Eq. (1) are quite rich. For instance, this equation captures long-wavelength secondary instabilities that may lead to an adjustment of the wave number k of the waves (Eckhaus instability), but also to spatiotemporal chaos if the Benjamin-Feir-Newell criterion

$$1 + c_1 c < 0 \quad (2)$$

is fulfilled. In this later case, very different dynamics involving specific localized structures are obtained depending on the precise values of c_1 and c , see e.g., Ref. [2]. This richness of behaviors, and the fact that simple generalizations of this equation appear to be also semiquantitatively valid for “large” ϵ in some cases [3], explains the interest of physicists in Eq. (1), as is evident from numerous reviews (e.g., Ref. [4]).

However, systematic comparisons of experiments and theories relying on Eq. (1) are sparse. This can be explained

on the one hand by the fact that the regime $\epsilon \rightarrow 0$, where (1) is expected to be quantitatively valid, is quite difficult to attain experimentally. On the other hand, the theoretical calculation of the coefficients of Eq. (1) from basic physical models is very demanding. A recent and interesting tentative comparison has focussed on the *traveling-wave wall modes* that are obtained in the *Rayleigh-Bénard convection of a rotating layer* of thickness h (Fig. 1) when the rotation rate Ω is sufficiently large, see e.g., Refs. [5,6] and references therein. The propagation of the waves is due to the Coriolis force, which dominates the viscous force as measured by the Coriolis number $\eta = 2h^2\Omega/\nu$, where ν is the kinematic viscosity of the fluid. In their remarkable experiments, Liu and Ecke [7,8] used water as fluid, corresponding to a Prandtl

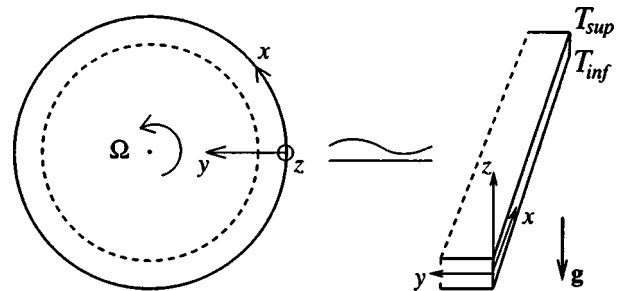


FIG. 1. Left, setup of the experiment of Liu and Ecke [7,8] as seen from above. Two isothermal horizontal disks separated at a distance h sandwich a layer of fluid, which is contained by a circular vertical sidewall. The whole apparatus is mounted on a table rotating at an angular velocity Ω around the axis of the disks. The dashed circle shows a virtual internal sidewall, which should not influence the wall modes at least for sufficiently large gaps (see text). Right, geometry of models based on a Cartesian approximation. Thus the sidewalls are unfolded to rectangles, and periodic boundary conditions are applied in the x direction.

TABLE I. The first line shows the critical Rayleigh number, wave number, and dimensionless frequency (see Sec. III), the coefficients or combinations of coefficients of the Ginzburg-Landau equation (1) measured experimentally by Liu and Ecke (LE) [8]. The Prandtl number $P=6.3$ corresponds to water at 25 °C, and the Coriolis number $\eta=548$. These measurements are compared with the theoretical predictions of Kuo and Cross (KC) [9] (second line) and of the present work (P) (third line). The discrepancies between the experiment and the theories are given in terms of percentages.

	R_c	k_c	ω_c	v_g	τ	ξ	$(c_0 - c_1)/\tau$	γ	$(c_0 - c)/\tau$
Expt. LE	20850	4.65	-22.0	2.65	0.03	0.179	4.2	0.74	20.4
Theor. KC	19500 - 6%	4.00 - 14%	-24.0 - 9%	2.22 - 16%	0.026 - 13%	0.24 - 34%	14.4 - 242%	1.11 - 50%	19.2 - 6%
Theor. P	19660 - 6%	4.22 - 9%	-22.4 - 2%	1.91 - 28%	0.025 - 16%	0.21 - 17%	6.40 - 52%	0.53 - 29%	19.7 - 3%

number P , the ratio of ν to the thermal diffusivity κ of the fluid, of 6.3. These experiments motivated the theoretical calculations of Kuo and Cross [9], Herrmann and Busse [10], Hecke and Saarloos [11]. All these authors neglected curvature effects and considered a Cartesian geometry. Because a wall mode is localized near a sidewall, it was suggested by Hecke and Saarloos that an experiment in an annular geometry should lead basically to the same results, as long as the gap between the two sidewalls is large as compared with the penetration length of the wall modes. Thus Hecke and Saarloos considered in Ref. [11] an annulus of finite aspect ratio $\Gamma = L_y/h$, where $y=0$ and $y=L_y$ locate the two sidewalls. A simpler semi-infinite geometry assuming $\Gamma = +\infty$ was considered in Refs. [9,10]. Only Kuo and Cross gave detailed predictions for the Ginzburg-Landau coefficients corresponding to the experiments of Liu and Ecke. The comparison shown in the first two lines of Table I is somehow disappointing, especially concerning the coefficients c_0 and c_1 which characterize the frequency shifts due to variations of the main control parameter ϵ and of the wave number k . The first goal of the present work is to reduce this discrepancy through the development of new models where fully rigid boundary conditions are used for the velocity field, instead of mixed conditions as in Refs. [9–11]. Indeed, to allow semi-analytical calculations, rigid boundaries were assumed only for the vertical sidewalls in Refs. [9–11], while unphysical stress-free horizontal boundaries were used. My more realistic models require fully numerical calculations from the beginning, based on the Fourier-Galerkin scheme presented in Appendix A, but lead to results closer to the experiments, as shown in the third line of Table I.

Another more fundamental motivation of this work concerns the form of the envelope equation in connection with the topology of the flow domain. At the nonlinear level, the envelope formalism requires an adiabatic elimination of the slaved modes of order of magnitude A^2 . Among those, a mean-flow mode can be excited if $|A|^2$ does not depend on the azimuthal coordinate x , or large-scale flow modes due to slow variations of $|A|^2$ in x . Usually, these two types of modes are calculated through the vorticity equation, i.e., the curl of the Navier-Stokes equation; this scheme is very convenient, since it permits a straightforward elimination of the pressure field. Hence these two types of modes give rise to the same type of contribution

$$|A(x,t)|^2 \mathbf{v}_{hmf}(y,z)$$

to the slaved velocity field. This is valid, in fact, in a singly connected domain such as that considered by Refs. [9,10]. On the contrary, in a multiply connected domain such as the annular domain considered in Ref. [11], according to the potential theory the Navier-Stokes equation is *not* equivalent to the vorticity equation. In order to insure the existence of the pressure field, this vorticity equation has to be supplemented with the azimuthal average of the azimuthal component of the Navier-Stokes equation [see Eq. (8) below]. This “global” equation does not enter into the calculation of modulated modes such as the linear modes relevant for the primary instability; but it must be solved at the nonlinear level for the mean-flow independent of x . This leads to a distinction between the two types of modes introduced above, and to contributions to the slaved velocity field of the form

$$\overline{|A(x,t)|^2} \mathbf{v}_{hmf}(y,z) + [|A(x,t)|^2 - \overline{|A(x,t)|^2}] \mathbf{v}_{lsf}(y,z).$$

The overbar designates the average in the azimuthal direction x , \mathbf{v}_{hmf} is the “homogeneous mean flow” and \mathbf{v}_{lsf} is the “large-scale flow.” Since the terms proportional to $|A|^2$ feed back on the active modes at order A^3 , one then obtains the *nonlocal* envelope equation

$$\begin{aligned} \tau(\partial_t A + v_g \partial_x A) &= (1 + ic_0)\epsilon A + \xi^2(1 + ic_1)\partial_x^2 A \\ &\quad - \gamma(1 + ic)|A|^2 A - \delta(1 + id)\overline{|A|^2} A. \end{aligned} \quad (3)$$

This new phenomenon [12], established for a two-dimensional model in Ref. [15], is studied here for the first time in a fully three-dimensional model. In particular, it will be shown that, in the limit of a large aspect ratio $\Gamma \rightarrow +\infty$ of the annular geometry considered, the nonlocal term in Eq. (3) does vanish, i.e., Eq. (1) is recovered.

The different models considered will be presented in Sec. II and the linear results in Sec. III. Section IV will establish envelope equation (3). The large-gap limit relevant to the experiments of Liu and Ecke will be discussed in Sec. V, and the small-gap case in Sec. VI.

II. MATHEMATICAL DESCRIPTION OF THE MODELS

Using the cell height h as length scale, the flow domain is defined by $x \in \mathbb{R}$, $y \in [0, \Gamma]$, $z \in [-1/2, 1/2]$ with a finite period L in the x direction (Fig. 1). Following Refs. [8–11], the

regime of not too large rotation rates is considered, where the centrifugal acceleration is negligible relative to the gravitational acceleration g . Time is scaled in units of the thermal diffusion time h^2/κ and temperature in units of $\kappa\nu/(\alpha gh^3)$, with the thermal expansion coefficient α of the fluid. Under the Boussinesq approximation, the evolution equations for the velocity \mathbf{v} and the deviation θ of the temperature from the basic profile of pure conduction are

$$P^{-1}[\partial_t \mathbf{v} + (\mathbf{v} \cdot \nabla) \mathbf{v}] + \eta \hat{\mathbf{z}} \times \mathbf{v} = -\nabla p + \Delta \mathbf{v} + \theta \hat{\mathbf{z}}, \quad (4)$$

$$\partial_t \theta + \mathbf{v} \cdot \nabla \theta = \Delta \theta + R v_z. \quad (5)$$

Here, in addition to the Prandtl number P and the Coriolis number η defined in the introduction, the Rayleigh number $R = \alpha g h^3 (T_{inf} - T_{sup}) / (\kappa \nu)$ and the pressure p appear. Because of the periodicity under $x \rightarrow x + L$ and of the incompressibility condition $\nabla \cdot \mathbf{v} = 0$, a spectral decomposition of the velocity field

$$\mathbf{v} = \hat{\mathbf{x}} v_0 + \hat{\mathbf{y}} (\partial_z \psi_0) - \hat{\mathbf{z}} (\partial_y \psi_0) + \sum_{k \in S} [i \hat{\mathbf{x}} (\partial_y v_{ky} + \partial_z v_{kz}) / k + \hat{\mathbf{y}} v_{ky} + \hat{\mathbf{z}} v_{kz}] e^{ikx} \quad (6)$$

can be used with $S = 2\pi \mathbb{Z}^* / L$, and with the functions v_0 , ψ_0 , v_{ky} , and v_{kz} depending only on y and z . Hereafter the limit of large L will be considered, where the wave numbers k vary quasicontinuously. As stated in the Introduction, because of the annular geometry the Navier-Stokes equation (4) is equivalent to the vorticity equation

$$P^{-1}[\partial_t \boldsymbol{\omega} + \mathbf{S}(\mathbf{v}, \mathbf{v})] - \eta \partial_z \mathbf{v} = \Delta \boldsymbol{\omega} + \hat{\mathbf{x}} (\partial_y \theta) - \hat{\mathbf{y}} (\partial_x \theta) \quad (7)$$

with $\boldsymbol{\omega} = \nabla \times \mathbf{v}$, $\mathbf{S}(\mathbf{v}, \mathbf{v}) = \nabla \times [(\mathbf{v} \cdot \nabla) \mathbf{v}]$, plus the x component of the Navier-Stokes equation (4) averaged in the x direction,

$$P^{-1}(\partial_t v_0 + \overline{\mathbf{v} \cdot \nabla v_x}) - \eta \partial_z \psi_0 = \Delta v_0. \quad (8)$$

For convenience, the local state vector of the fluid

$$V = (v_x, v_y, v_z, \theta) = (\mathbf{v}, \theta)$$

is introduced, and Eqs. (5) and (7) relevant for x -dependent modes ($k \neq 0$) are written in the form

$$D \partial_t V + N_2(V, V) = L_R V, \quad (9)$$

where D, L_R (N_2) are linear (nonlinear) operators.

Realistic rigid boundary conditions,

$$\mathbf{v} = \mathbf{0} \quad \text{for } y = 0, \Gamma, \quad z = \pm 1/2,$$

are used for the velocity field. With spectral decomposition (6), they translate into

$$v_0 = \psi_0 = v_{ky} = v_{kz} = 0 \quad \text{for } y = 0, \Gamma, \quad z = \pm 1/2,$$

$$\partial_y \psi_0 = \partial_y v_{ky} = 0 \quad \text{for } y = 0, \Gamma, \quad (10)$$

$$\partial_z \psi_0 = \partial_z v_{kz} = 0 \quad \text{for } z = \pm 1/2.$$

Whereas the horizontal plates are always assumed perfectly conducting, i.e.,

$$\theta = 0 \quad \text{for } z = \pm 1/2, \quad (11)$$

three different types of thermal boundary conditions have been implemented at the sidewalls. Model CC, used for validation by comparison with Ref. [16], assumes sidewalls that are also perfectly conducting,

$$\theta = 0 \quad \text{for } y = 0, \Gamma. \quad (12)$$

Models II and CI, on the other hand, have been developed to approximate the experimental boundary conditions of Liu and Ecke, where the ratio of the thermal conductivity of the sidewall to that of the fluid was of the order of 0.25, i.e., small. For the purpose of simplification, and following Ref. [11], it is assumed in model II that this ratio vanishes, i.e., that the two sidewalls are insulating:

$$\partial_y \theta = 0 \quad \text{for } y = 0, \Gamma. \quad (13)$$

This, however, leads to the existence of two counterpropagating sidewall modes, each one attached to one of the sidewalls. Therefore, the competition between these two modes should be analyzed first, presumably with two coupled envelope equations generalizing (1). Because the form and the validity of such envelope equations is still the object of a controversy (see, e.g., the discussion in Ref. [17]), it seems interesting to develop also an asymmetric model CI with an internal conducting sidewall and an external insulating sidewall:

$$\theta = 0 \quad \text{for } y = \Gamma, \quad \partial_y \theta = 0 \quad \text{for } y = 0. \quad (14)$$

This asymmetric model favors external sidewall modes (see Ref. [10] and Sec. III), and moreover permits a simpler Galerkin ansatz for the temperature field [see Eq. (A8)].

III. LINEAR RESULTS: PROPERTIES OF THE SIDEWALL MODES

With the Fourier-Galerkin scheme introduced in Appendix A, the linearized version of Eq. (9),

$$\sigma(k, n, R) D V_1(k, n, R) = L_R V_1(k, n, R) \quad (15)$$

with $V_1(k, n, R)$ depending on x only through the factor $\exp(ikx)$, is transformed to a matrix eigenvalue problem. The eigenvalues $\sigma(k, n, R)$, depending on the wave number $k \neq 0$ and on a mode number n , are computed, and neutral modes verifying $\text{Re}(\sigma) = 0$ are sought. They correspond to $R = R_0(k, n)$; by minimizing these functions with respect to k , the optimal modes $V_1(k_c^n, n, R_c^n)$ are found. The corresponding eigenvalues $\sigma(k_c^n, n, R_c^n)$ assume the form $-i\omega_c^n$, with the optimal frequencies ω_c^n . A further minimization of the corresponding thresholds R_c^n yields the critical value n_c of n . The corresponding values of $R_c^{n_c}$ ($k_c^{n_c}$), more simply noted R_c (k_c), are the critical Rayleigh number (wave number); the corresponding optimal mode is called the critical mode; the corresponding frequency is the critical frequency

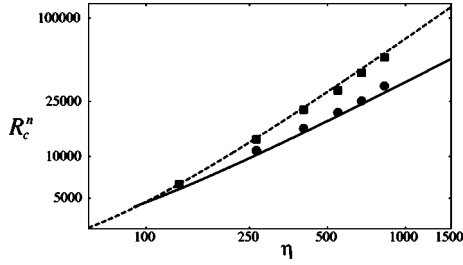


FIG. 2. For $P=6.3$, the dashed line shows the onset values R_c^b of the stationary bulk mode in infinite geometry calculated with the scheme of Ref. [18]. The squares show the corresponding measurements of Liu and Ecke [8]. For Coriolis numbers $\eta \gtrsim 100$, traveling-wave sidewall modes are excited at a lower Rayleigh number R_c^e . The corresponding onset values calculated with the Galerkin code are shown with the full line, whereas the disks show the measurements of Liu and Ecke.

ω_c . For fixed control parameters P , η , Γ , the results of the computations are considered to be ‘‘Galerkin converged’’ if the relevant values of k_c^n , R_c^n , and ω_c^n change by less than 1.5% when the truncation parameter N of the Galerkin code [see Eq. (A10)] is increased by two. Note that all the active modes discussed hereafter are *even modes* such that, under $z \mapsto -z$,

$$v_z \text{ and } \theta \text{ are even, } v_x \text{ and } v_y \text{ are odd.} \quad (16)$$

With model CC, and a vanishing Coriolis number like in Ref. [16], the critical mode is a stationary bulk mode which invades the whole gap $0 < y < \Gamma$. The results of Table I of Ref. [16] are recovered with a very good accuracy.

With models II and CI, sidewall modes become preferred for not too small values of η ; the computation of a sidewall branch is considered to be converged if the corresponding Galerkin converged values of k_c^n , R_c^n , and ω_c^n change by less than 1.5% when Γ is increased by one unit. Figure 2 shows the onset values $R_c = R_c^e$ corresponding to the external insulating-sidewall modes (which are identical in models II and CI), together with the bulk mode onset values R_c^b in infinite geometry for the purpose of completeness. A good agreement is obtained with the measurements of Liu and Ecke [8]. With model CI, the inner conducting-sidewall modes can also be computed. These modes become neutral only at quite large values R_c^i of the Rayleigh number. For instance, for $P=6.3$, $\eta=1000$, I find $R_c^e = 34\,520$ and $R_c^i = 67\,580$, of the order of magnitude of $R_c^b = 71\,080$. This fact that a conducting sidewall dramatically damps wall modes agrees with the results of Herrmann and Busse [10]. Hence, in the following, I shall focus on the external insulating-wall modes. The numerical values of R_c^e in Fig. 2 indicate a scaling law of the form $R_c^e \propto \eta$ for large η , in accordance with [9,10]. As shown in Fig. 3(a), the critical wave number k_c^e of the sidewall modes converges to a finite value when $\eta \rightarrow \infty$; this behavior also agrees with the results of Refs. [9,10]. With their negative frequency ω_c^e [Fig. 3(b)], the external sidewall modes do correspond to waves traveling in the retrograde direction. The comparison of Fig. 3(b) with

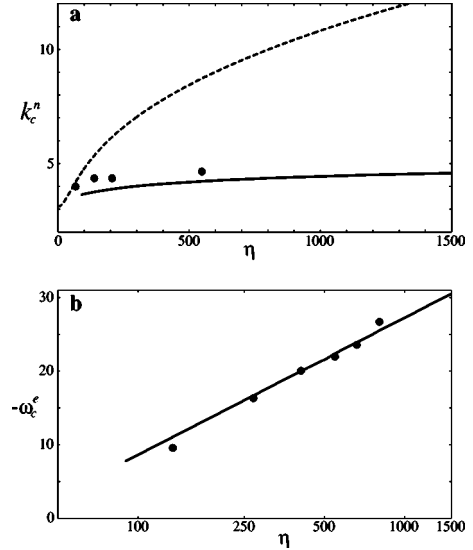


FIG. 3. (a) For $P=6.3$, the dashed line shows the optimal values k_c^b of the azimuthal wave number of the stationary bulk mode in infinite geometry. The full line shows the critical wave number k_c^e of the sidewall mode computed with the Galerkin code, and the disks show the corresponding measurements of Liu and Ecke [8]. (b) Under the same conditions, the computed critical frequencies are compared with those measured by Liu and Ecke.

the Fig. 4 of [8] also shows that the agreement between the computed and measured frequencies is much better than in the case of the mixed model [9]; see also the first columns of Table I for such comparisons. The numerical results of Fig. 3(b) indicate a peculiar scaling law for the frequency ω_c^e which appears to be proportional to $\ln \eta$. This property contrasts with the results of the mixed model [9,10], where it was found that ω_c^e converges to a limit value for $\eta \rightarrow \infty$.

Another relevant difference with respect to previous analyses is that, with the model II, bulk modes are never found to become critical for $\eta > 100$, in contradiction to the findings of Hecke and Saarloos [11]. They predicted that for $P=0.15$ and $\Gamma=1$, traveling-waves bulk modes become critical for $280 \lesssim \eta \lesssim 11\,200$. With $P=0.15$ and $\Gamma=1$, I do find traveling-waves bulk modes with rather large wave numbers as in Ref. [11], but they correspond to a value of $R_c^n > 1.7R_c^e$. This large discrepancy cannot solely be due to the different velocity boundary conditions. It reveals an error in the linear scheme of Hecke and Saarloos: they assumed that the x and y components of the vorticity equation imply its z component, which was not solved (see Ref. [19] p. 35). In fact, still for $\Gamma=1$ and at even lower Prandtl numbers, it turns out that the most dangerous modes after the sidewall modes are oscillatory axisymmetric bulk modes (corresponding to the continuous limit $k \rightarrow 0$) rather analogous to those presented in Ref. [20]. For instance, for the Prandtl number of liquid mercury $P=0.0257$, the corresponding ratio R_c^n/R_c^e attains a minimum of 1.23 for $\eta=630$.

IV. WEAKLY NONLINEAR ENVELOPE EQUATION

In the weakly nonlinear regime, where $\epsilon = R/R_c - 1 \ll 1$, approximate solutions of the evolution equations (8) and (9)

can be obtained with the so-called weakly nonlinear methods. Here the spectral approach exposed, for instance, in Refs. [15,21] is employed. The basic ansatz assumes the form

$$V = W + W^* + V_{\perp} \quad (17)$$

with

$$W = \sum_{q \ll k_c} \hat{A}(k_c + q) V_1(k_c + q) e^{-i\omega_c t} \quad (18a)$$

$$\sim \sum_{q \ll k_c} \hat{A}(k_c + q) V_1(k_c) e^{i(qx - \omega_c t)} \quad (18b)$$

$$\sim A(x) V_1(k_c) e^{-i\omega_c t} \quad (18c)$$

being the active wave packet, and V_{\perp} , regarded as a perturbation of W , in the passive modes subspace generated by the eigenmodes of linearized problem (15) with finite negative growth rate $\text{Re}(\sigma)$. In Eq. (18), $V_1(k_c + q)$ is the neutral mode of wave number $k_c + q$,

$$V_1(k_c) = (\mathbf{v}_1(x, y, z), \theta_1(x, y, z)) = (\tilde{\mathbf{v}}_1(y, z), \tilde{\theta}_1(y, z)) e^{ik_c x} \quad (19)$$

is the critical mode, and

$$A(x) = \sum_{q \ll k_c} \hat{A}(k_c + q) e^{iqx} \quad (20)$$

is the slowly varying envelope. The first step of the nonlinear calculations consists of the “adiabatic” elimination of V_{\perp} at order A^2 ; for the calculation of the corresponding nonlinear terms, the simplified forms (18b) and (18c) of W can be used. Because of the properties of symmetry of Eqs. (8) and (9), all the contributions to V_{\perp} that will now be calculated have a z symmetry opposite to that of the active linear modes (16): they are *odd modes* such that, under $z \mapsto -z$,

$$v_z \text{ and } \theta \text{ are odd, } v_x \text{ and } v_y \text{ are even.} \quad (21)$$

A. Elimination of the homogeneous mode

The mode of temperature and velocity in V_{\perp} which is homogeneous with respect to x assumes the form

$$\sum_q \hat{A}(k_c + q) \hat{A}(-k_c - q) V_2^h = \overline{|A(x)|^2} V_2^h \quad (22)$$

with $V_2^h = V_2^h(y, z) = (v_x^h, \partial_z \psi^h, -\partial_y \psi^h, \theta^h)$, using the notation

$$\hat{A}(-k_c - q) = \hat{A}^*(k_c + q).$$

It is controlled by the averaged azimuthal Navier-Stokes equation (8), the averaged azimuthal vorticity equation (7) $\cdot \hat{\mathbf{x}}$, and the averaged heat equation (5) at order of magnitude A^2 ,

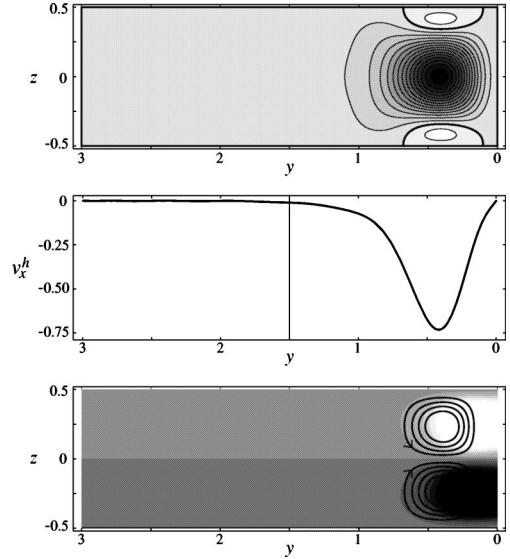


FIG. 4. Homogeneous mode $A_0^2 V_2^h$ computed for $P=6.3$, $\eta = 200$, $\Gamma=3$, $\epsilon=0.1$, and the model II. Upper plot: contour lines of the azimuthal velocity $v_x^h(y, z)$. The thick line is the isoline $v_x^h = 0$. Mid plot: profile of $A_0^2 v_x^h(y, 0)$ vs y . Bottom plot: the contour lines of the temperature field $\theta^h(y, z)$ are shown with the gray levels, and the transverse flow lines, i.e., the isolines of $\psi^h(y, z)$ are shown with the full lines. The arrows indicate the direction of the transverse flow. The maximum value of $A_0^2 \theta^h(y, z)$ is 288.

$$\mu \text{Re}(\mathbf{v}_1 \cdot \nabla v_{1x}^*) = \Delta v_x^h + \eta \partial_z \psi^h, \quad (23a)$$

$$\mu \text{Re}[S_x(\mathbf{v}_1, \mathbf{v}_1^*)] = -\Delta \Delta \psi^h + \eta \partial_z v_x^h + \partial_y \theta^h, \quad (23b)$$

$$2 \text{Re}(\mathbf{v}_1 \cdot \nabla \theta_1^*) = \Delta \theta^h - R_c \partial_y \psi^h, \quad (23c)$$

with the notation $\mu = 2/P$. Note that, because of the identities

$$S_y(\mathbf{v}_1, \mathbf{v}_1^*) = \partial_z[(\mathbf{v}_1 \cdot \nabla) v_{1x}^*], \quad (24a)$$

$$S_z(\mathbf{v}_1, \mathbf{v}_1^*) = -\partial_y[(\mathbf{v}_1 \cdot \nabla) v_{1x}^*], \quad (24b)$$

the derivatives of Eq. (23a) with respect to y and z yield the y and z components of the averaged vorticity equation (7). The system (23) is solved numerically with the Galerkin scheme. A representative result, normalized physically with the use of $A = A_0$ given by Eq. (43a), is shown in Fig. 4. A retrograde flow is generated near the external sidewall. This flow is small but not negligible as compared with the leading-order flow: with the parameters of Fig. 4, the maximum value of $A_0^2 |v_x^h|$ is only 11.6 times smaller than the maximum value of $2A_0 \text{Re}(v_{1z})$. Note also the classical heating (cooling) of the upper (lower) part of the layer due to convection near the sidewall.

B. Elimination of the large-scale modes

The large-scale modes in V_{\perp} are generated by the nonlinear term

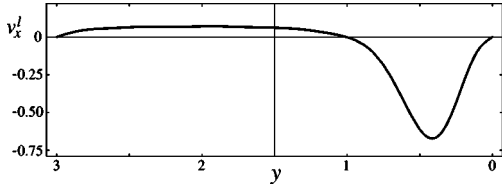


FIG. 5. For the parameters of Fig. 4, the azimuthal component of the large-scale flow $A_0^2 v_x^l(y, 0)$ in the middle of the layer is plotted vs y .

$$\sum_q \sum_{q' \neq q} \hat{A}(k_c + q) \hat{A}(-k_c - q') \times N_2(V_1(k_c) e^{iqx} | V_1(-k_c) e^{-iq'x})$$

in Eq. (9), where the notation

$$N_2(V_a | V_b) = N_2(V_a, V_b) + N_2(V_b, V_a)$$

has been used. Their elimination yields to lowest order

$$V_\perp^l = \sum_q \sum_{q' \neq q} \hat{A}(k_c + q) \hat{A}(-k_c - q') V_2^l e^{i(q-q')x} = [|A(x)|^2 - \overline{|A(x)|^2}] V_2^l \quad (25)$$

with $V_2^l = V_2^l(y, z) = (v_x^l, v_y^l, v_z^l, \theta^l)$ defined by

$$V_2^l = \lim_{q \rightarrow 0} L_{R_c}^{-1} N_2(V_1(k_c) e^{iqx} | V_1(-k_c)). \quad (26)$$

This limit, which has to be taken for $q \neq 0$, and which is real, is computed numerically with the Fourier-Galerkin scheme. Note that the continuity equation

$$iqv_x^l + \partial_y v_y^l + \partial_z v_z^l = 0 \quad (27)$$

implies the constraint

$$\int_0^\Gamma \int_{-1/2}^{1/2} v_x^l(y, z) dy dz = 0, \quad (28)$$

which has no counterpart in the properties of the homogeneous flow. From Eq. (28), it is clear that the large-scale flow cannot be purely retrograde as is nearly the case for the homogeneous flow (Fig. 4). Indeed, Fig. 5 shows the existence of a prograde component of the flow throughout most of the interior of the layer. It is thus erroneous to assume that V_2^h and V_2^l are identical, as has been done in Ref. [11]. In order to prove this in more details and to isolate the nonlocal effects [see Eq. (32)], I focus now on the difference $V_2^h - V_2^l$. For this purpose, it is worthwhile to note that limit (26) satisfies the following equations derived from the vorticity and heat equations (7) and (5), i.e., the components of Eq. (9),

$$\mu \text{Re}[S_x(\mathbf{v}_1, \mathbf{v}_1^*)] = \Delta(\partial_y v_z^l - \partial_z v_y^l) + \eta \partial_z v_x^l + \partial_y \theta^l, \quad (29a)$$

$$\mu \text{Re}[S_y(\mathbf{v}_1, \mathbf{v}_1^*)] = \Delta(\partial_z v_x^l) + \eta \partial_z v_y^l, \quad (29b)$$

$$\mu \text{Re}[S_z(\mathbf{v}_1, \mathbf{v}_1^*)] = -\Delta(\partial_y v_x^l) + \eta \partial_z v_z^l, \quad (29c)$$

$$2 \text{Re}(\mathbf{v}_1 \cdot \nabla \theta_1^*) = \Delta \theta^l + R_c v_z^l. \quad (29d)$$

C. Difference between these modes: Global mode

From continuity equation (27) in the large-scale limit $q \rightarrow 0$, one expects the existence of a large-scale stream function ψ^l such that

$$v_y^l = \partial_z \psi^l \quad \text{and} \quad v_z^l = -\partial_y \psi^l. \quad (30)$$

The global mode is defined as the difference

$$v_x^g = v_x^h - v_x^l, \quad \psi^g = \psi^h - \psi^l, \quad \theta^g = \theta^h - \theta^l, \quad (31)$$

i.e., $V_2^g = (v_x^g, \partial_z \psi^g, -\partial_y \psi^g, \theta^g) = V_2^h - V_2^l$, such that the sum of homogeneous (22) and large-scale modes (25) in V_\perp reads

$$V_\perp^{hl} = \overline{|A(x)|^2} V_2^g + |A(x)|^2 V_2^l. \quad (32)$$

By comparison of Eqs. (29b) and (29c) with Eq. (23a), the identities (24) show that

$$\partial_y (\Delta v_x^g + \eta \partial_z \psi^g) = \partial_z (\Delta v_x^g + \eta \partial_z \psi^g) = 0,$$

i.e.,

$$\Delta v_x^g + \eta \partial_z \psi^g = M. \quad (33a)$$

On the other hand, subtraction of Eq. (29a) from Eq. (23b) and of Eq. (29d) from Eq. (23c) yields

$$-\Delta \Delta \psi^g + \eta \partial_z v_x^g + \partial_y \theta^g = 0, \quad (33b)$$

$$\Delta \theta^g - R_c \partial_y \psi^g = 0. \quad (33c)$$

The three equations (33) show that the global mode corresponds to the velocity and temperature fields that a constant pressure gradient M in the x direction would drive; of course the value of M is not free but set by the difference V_2^g between the nonlinear modes V_2^h and V_2^l computed in Secs. IV A and IV B (see Appendix A 2 for details on these computations). A typical result for V_2^g , which will be commented on in Sec. V, is shown in Fig. 6.

D. Elimination of the short-scale modes

As usual, the nonlinear source terms of wave numbers close to $\pm 2k_c$ generate the terms

$$V_\perp^s = A^2(x) V_2^s \exp(-2i\omega_c t) + \text{c.c.} \quad (34)$$

in V_\perp , where V_2^s depends on x through the factor $\exp(2ik_c x)$. This finishes the determination of the passive modes at lowest order, which thus yields

$$V_\perp = V_\perp^{hl} + V_\perp^s. \quad (35)$$

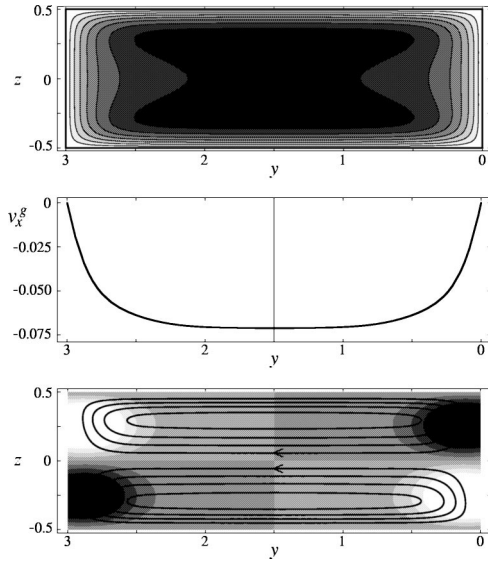


FIG. 6. Same as Fig. 4, but for the global mode $A_0^2 V_2^g$, i.e., the fields $v_x^g(y, z)$, $A_0^2 v_x^g(y, 0)$, $\theta^g(y, z)$, and $\psi^g(y, z)$ from top to bottom. The maximum value of $A_0^2 \theta^g(y, z)$ is 0.93.

E. Envelope equation

The linear terms of the envelope equation are obtained as in Ref. [15] from the expansion

$$\sigma(k_c + q, n_c, R) \sim -i(\omega_c + v_g q) + \tau^{-1}[(1 + ic_0)\epsilon - \xi^2(1 + ic_1)q^2]$$

of the linear eigenvalue for small q and ϵ , where v_g is the group velocity of the waves, and $\tau(\xi)$ is the characteristic time (length) of the instability. On the other hand, the resonant nonlinear terms in Eq. (9), which are contained in $N_2(W|V_\perp) + N_2(W^*|V_\perp)$, yield after projection onto the adjoint critical mode U_1^c the terms

$$-\tau^{-1}\gamma(1 + ic)|A(x)|^2 A(x) - \tau^{-1}\delta(1 + id)\overline{|A(x)|^2 A(x)}$$

with

$$\tau^{-1}\gamma(1 + ic) = \langle N_2(V_1(k_c)|V_2^l) + N_2(V_1(-k_c)|V_2^s), U_1^c \rangle, \quad (36a)$$

$$\tau^{-1}\delta(1 + id) = \langle N_2(V_1(k_c)|V_2^g), U_1^c \rangle. \quad (36b)$$

After adding the linear terms and multiplying by τ , one obtains envelope equation (3). For fixed values of the control parameters P , η , and Γ , the numerical values of the coefficients of Eq. (3) are considered to be Galerkin converged if they change by less than 2.5% when the truncation parameter N (A10) is increased by 2.

F. Source terms controlling the homogeneous and large-scale flows—validations

The nonlinear source term in homogeneous flow equation (23a) assumes the form

$$\begin{aligned} \mu \text{Re}(\mathbf{v}_1 \cdot \nabla v_{1x}^*) &= 2(Pk_c)^{-1} \text{Im}[\tilde{v}_{1y} \partial_y (\partial_y \tilde{v}_{1y}^* + \partial_z \tilde{v}_{1z}^*) \\ &+ \tilde{v}_{1z} \partial_z (\partial_y \tilde{v}_{1y}^* + \partial_z \tilde{v}_{1z}^*)]. \end{aligned} \quad (37)$$

Because of Eq. (24), the derivatives of this expression with respect to y and z are also the nonlinear source terms in large-scale equations (29b) and (29c). In the absence of rotation and for bulk modes, the critical eigenfunctions \tilde{v}_{1y} and \tilde{v}_{1z} can be chosen to be real; consequently these source terms vanish. Since $\eta = 0$, Eqs. (23a), (29b), and (29c) show that $v_x^h = v_x^l = 0$. Thus $v_x^g = 0$, and according to Eq. (33a) $M = V_2^g = 0$ as assumed in Ref. [16]. With the Galerkin code for model CC, the local envelope equation (4.13) of [16] is recovered, with values of the coefficients in very good agreement with those of Table I of Ref. [16].

On the contrary, in the presence of rotation and for sidewall modes, the critical eigenfunctions \tilde{v}_{1y} and \tilde{v}_{1z} are always complex. Thus nonlinear source term (37) and its derivatives are nonvanishing, as are v_x^h (Fig. 4), v_x^l (Fig. 5), and hence v_x^g (Fig. 6). Before proceeding with the description of the nonlinear results, I mention that a validation of full envelope equation (3) has been done through a comparison of the results of the stability analysis of the critical solution of Eq. (3) with respect to long-wavelength modulations (see Sec. 4.3 of Ref. [15]) with a direct numerical stability analysis based on computations similar to those of Appendix C of Ref. [22]. A very good agreement has been obtained.

V. LARGE-GAP LIMIT

Equations (33) are invariant under $y \mapsto \Gamma - y$. Thus with model II, the boundary conditions of which are also symmetrical, one has under $y \mapsto \Gamma - y$ that

$$v_x^g \text{ and } \psi^g \text{ are even, } \theta^g \text{ is odd.} \quad (38)$$

Because it is driven by a (virtual) pressure gradient independent of y and z , the global mode is a bulk mode which invades the whole gap, as shown in Fig. 6. This figure, as Figs. 4 and 5, has been computed with model II. With model CI, the fields are very similar and only weakly affected, near the internal sidewall, by the different thermal boundary conditions. From an energetic point of view, it is clear that the sidewall modes cannot feed a large amplitude global mode invading the whole gap, especially in the large-gap limit. Indeed, the numerical results show that the ratio of the maximum values of $|v_x^g|$ and $|v_x^h|$, or equivalently of the maximum values of θ^g and θ^h , decay rapidly with increasing Γ . Accordingly, the ratio of the global-coupling term $\delta(1 + id)$ (36b) vs the local-coupling term $\gamma(1 + ic)$ (36a) decays rapidly with increasing Γ . This is shown in Fig. 7 for the real parts of these coefficients; note that the critical mode has been normalized with the convention defined by Eq. (28) of [8], i.e., such that the reduced Nusselt number reads

$$\text{Nu} - 1 = 0.36|A|^2 + O(A^4). \quad (39)$$

The data of Fig. 7 indicate a power-law decrease of δ vs Γ with an exponent of the order of -1.1 . The numerical results

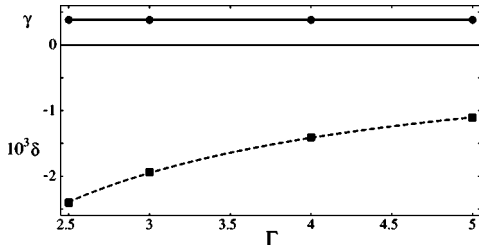


FIG. 7. For $P=6.3$, $\eta=200$, the disks show the computed values of the local saturation coefficient γ vs the dimensionless gap Γ . These values have already converged to their limit value for $\Gamma \rightarrow +\infty$ shown by the full line. The squares show the (rescaled) nonlocal saturation coefficient δ ; the dashed line is a fit of these data to a power law.

show a similar behavior of the imaginary parts γc and δd of coefficients (36a) and (36b), with the same exponent for the power law of δd vs Γ . Naturally models II and CI give the same results. Thus the limit $\Gamma \rightarrow +\infty$ is regular, and local envelope equation (1) used in Refs. [7–9] is recovered in the large-gap limit, with the coefficients shown in the last line of Table I for $P=6.3$, $\eta=548$. The remaining discrepancies with the experiments are probably due to the finite thermal conductivity of the sidewall and due to curvature effects (the experiments were carried out in a disk with a not very large radius-to-height ratio of five).

VI. SMALL-GAP CASE

A natural question arising from this work concerns the possibility of new experiments in an annular geometry that may exhibit the nonlocal term of Eq. (3). It is obvious from Fig. 7 that a small gap should be used. Asymmetric boundary conditions corresponding to model CI, with an inner conducting sidewall and an external insulating sidewall, should be of interest: then only external sidewall modes will become critical for $\eta \gtrsim 100$, and more complicated effects generated by the competition between left and right traveling waves will not appear. The next important point concerns the measurable effects of the nonlocal nonlinear term is Eq. (3). This term sums up with the local nonlinear term for monochromatic waves

$$A = A_q \exp[i(qx - \tilde{\omega}t)], \quad (40)$$

for which $\overline{|A|^2} = |A|^2$. Hence for such waves envelope equation (3) reduces to the local envelope equation of the form (1)

$$\begin{aligned} \tau(\partial_t A + v_g \partial_x A) &= (1 + ic_0)\epsilon A + \xi^2(1 + ic_1)\partial_x^2 A \\ &\quad - g_3(1 + ic_3)|A|^2 A \end{aligned} \quad (41)$$

with

$$g_3 = \gamma + \delta, \quad c_3 = (\gamma c + \delta d)/g_3. \quad (42)$$

The corresponding solutions read

$$A_q = \sqrt{[\epsilon - \epsilon_0(q)]/g_3}, \quad (43a)$$

$$\tilde{\omega} = [(c_3 - c_0)\epsilon + \tau v_g q + \xi^2(c_1 - c_3)q^2]/\tau, \quad (43b)$$

and exist only for

$$\epsilon > \epsilon_0(q) = \xi^2 q^2. \quad (44)$$

Obviously, detailed measurements of the amplitude and frequency of these waves yield estimates of the coefficients of Eq. (41) as in Ref. [8]. The study of the Eckhaus instability may then reveal the nonlocal effects. Indeed, from the local envelope equation (41), one would expect an Eckhaus limit at

$$\epsilon_E(q) = \frac{2(1 + c_3^2) + 1 + c_1 c_3}{1 + c_1 c_3} \epsilon_0(q). \quad (45)$$

However, the full nonlocal envelope equation (3) yields a different result (see Ref. [23] for the calculation of this limit)

$$\epsilon'_E(q) = \frac{2(1 + c^2) \left(1 + \frac{\delta}{\gamma}\right) + 1 + c_1 c}{1 + c_1 c} \epsilon_0(q). \quad (46)$$

Taking into account the fact that $\delta \ll \gamma$ (Fig. 7), one sees that the difference between $\epsilon_E(q)$ and $\epsilon'_E(q)$ corresponds essentially to the replacement of c_3 by c . Since $c_3 - c = \delta(d - c)/g_3$, this change will be important if δ/γ is not too small and if δd is quite different from δc . As shown in Figs. 8(a) and 8(b), this happens only for very small Prandtl numbers $P < 0.05$. Indeed important global effects require a large-amplitude global-mean flow, i.e., a weak viscous damping, i.e., a small viscosity, see the factors of P^{-1} in front of the nonlinear advection terms like Eq. (37). It is also important to note that the global coefficient δ does not vary monotonically with P [Fig. 8(a)], indicating complex changes in the structure of the flows; for instance, the form of the homogeneous flow depends strongly on the Prandtl number as shown in Fig. 9 (compare with Fig. 4). Figures 8(a) and 8(b), which suggest that the limit $P \rightarrow 0$ is singular, can be complemented by the plots of $\epsilon_E(q)/\epsilon_0(q)$ and $\epsilon'_E(q)/\epsilon_0(q)$ shown in Fig. 8(c). For the exhibition of global effects, the use of a liquid metal such as liquid mercury corresponding to $P=0.0257$ [24] appears to be appropriate. For $P=0.0257$, $\Gamma=1$, $\eta=250$, model CI predicts $\gamma=11.10$, $\delta=-0.901$, $c_1=-0.151$, $c=-0.011$, and $c_3=-1.067$, i.e., a ratio $\epsilon'_E(q)/\epsilon_E(q)$ of 0.605. This significant decrease of the Eckhaus limit as compared with the predictions of the local envelope equation should be measurable experimentally. This calculation furthermore reveals the stabilizing effect of the nonlocal term on modulational instabilities at very small Prandtl number. Indeed, in contradiction to Ref. [11], I find no region of Benjamin-Feir instability in this system; since $\gamma > 0$ always holds, the corresponding criterion for modulational stability is $1 + c_1 c > 0$, see Ref. [15] or [23].

VII. CONCLUSION

The occurrence of global coupling from the “topological” constraint (8) is an interesting result, that extends the previ-

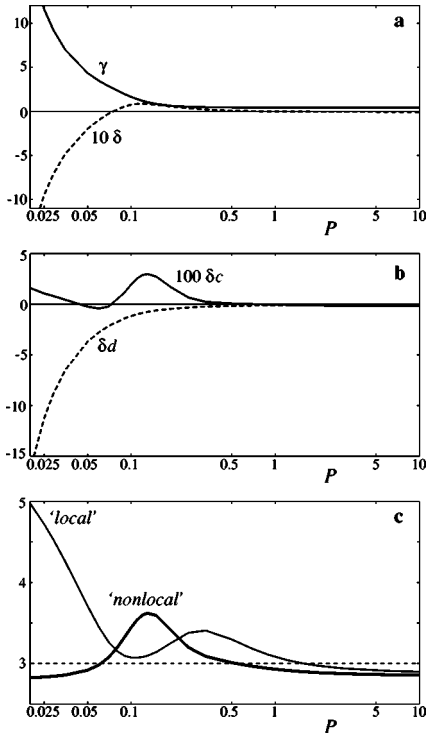


FIG. 8. For $\Gamma = 1$, $\eta = 250$, (a) shows the value of the local (full line) and (rescaled) nonlocal (dashed line) saturation coefficients γ and δ versus the Prandtl number P ; (b) shows the value of the (rescaled) local (full line) and nonlocal (dashed line) frequency-shift coefficients c and d after a multiplication by δ . (c) The thin line shows the value of the reduced Eckhaus-instability threshold $\epsilon'_E(q)/\epsilon_0(q)$ (45) that one would expect on the basis of the effective local envelope equation (41). The thick line shows the correct threshold $\epsilon'_E(q)/\epsilon_0(q)$ (46) predicted by the full nonlocal envelope equation (3). The thin dashed line shows for memory the classical value obtained when the frequency-shift coefficients vanish.

ous analysis [15] restricted to a two-dimensional system. Physically, the generation of the mean and large-scale flows originates from the nonlinear advection term or Reynolds-stress term $(\mathbf{v} \cdot \nabla)\mathbf{v}$ in the Navier-Stokes equation. Because

their x dependence can be described as the sum of Fourier modes in $\exp(iqx)$ with $q \neq 0$, the large-scale flows automatically fulfill the requirement of a vanishing mean pressure gradient in the x direction, and can be calculated with the vorticity equation. By contrast, the strictly homogeneous mean flow has to adjust in accordance with this requirement, i.e., it has to be calculated directly with the Navier-Stokes equation. Since the corresponding nonlinear source terms can be deduced by the application of the curl operator, the difference $V_2^g(y, z)$ between the homogeneous and large-scale flow modes $V_2^h(y, z)$ and $V_2^l(y, z)$, i.e., the global mode factor of $|A(x)|^2$ in V_\perp , is a neutral mode of the linearized vorticity equation [as confirms the inspection of Eqs. (33a) and (33b)]. This explains why a scheme relying only on the vorticity equation, like that of Ref. [11], cannot capture this global mode. This also shows why the global flow must equilibrate a mean pressure gradient M in the x direction. A further important result is that the magnitude of the mean, large-scale, and global flows, and of the corresponding global-coupling coefficients, is controlled by the viscous damping: the smaller the viscosity, i.e., the Prandtl number, the stronger the mean flows, see Figs. 8(a) and 9(b). This classical tendency was also found in a similar context in Ref. [15], see e.g. its Fig. 4(b). It is, moreover, interesting to quote that the nonlocal effects do not enter for monochromatic waves, for which the local envelope equation (41) is effectively valid; indeed the corresponding nonlinear term,

$$\tau^{-1} g_3(1 + ic_3) = \langle N_2(V_1(k_c)|V_2^h) + N_2(V_1(-k_c)|V_2^g), U_1^c \rangle$$

because of $V_2^l + V_2^g = V_2^h$, can be calculated from the knowledge of V_2^h (and V_2^g) ignoring both V_2^l and V_2^g . Naturally, the nonlocal effects enter only for more general solutions such that $|A(x)|^2 \neq |A(x)|^2$, e.g., modulated solutions. Indeed the nonlocal effects alter the modulational Eckhaus instability as shown in Fig. 8(c); this may permit experiments exhibiting the nonlocal effects, as discussed at the end of Sec. VI.

Global-coupling effects similar to those exhibited here exist, in principle, in any hydrodynamical annular system. Yet, they are quite probably negligible in many situations, as in the present case for fluids with Prandtl numbers $P \geq 1$. From a direct analogy, it is thus expected that the use of local envelope equations is justified for the analyses of the binary-mixture experiments [25,26], since the Prandtl number was larger than six in both experiments. The qualitative use of local models for convection experiments in gases [27,28] also appears to be justified, since the Prandtl number $P \geq 0.7$. However, Fig. 8(c) suggests that high-precision convection experiments in gases may reveal nonlocal effects. Another classical annular setup used for the study of hydrodynamic instabilities is the Taylor-Couette apparatus. In this system global-coupling effects should also exist, as pointed out by Refs. [13] and [14]; it would be interesting to revisit these pioneering studies.

It is finally important to mention that nonlinear and nonlocal waves represent a category of phenomena that go beyond hydrodynamics. For instance, it has been shown recently [23] that the envelope equation for ionization waves in

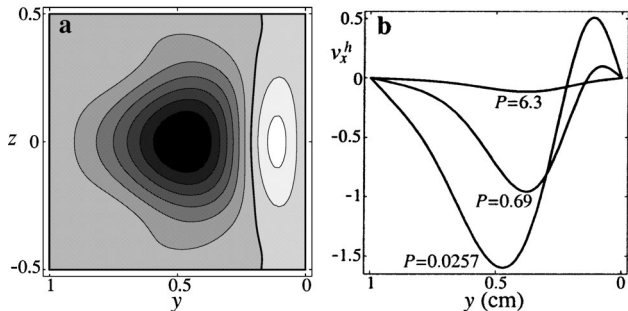


FIG. 9. (a) Contour lines of the homogeneous azimuthal flow $v_x^h(y, z)$ computed for $P = 0.0257$, $\Gamma = 1$, $\eta = 250$. The thick line is the isoline $v_x^h = 0$. (b) for $\Gamma = 1$, $\eta = 250$, and $\epsilon = 0.1$ corresponding to water, pressurized argon and mercury from top to bottom [24], profiles of the dimensional azimuthal flow $(\kappa/h)A_0^2 v_x^h(y, 0)$ vs y predicted for a cell of thickness $h = 1$ cm. One unit of the vertical axis is 0.1 mm/s.

a plasma column is nonlocal, because the constraint of a fixed electric potential assumes the nonlocal form

$$\int_0^L E_x dx = U - RI$$

with \mathbf{E} being the electric field (compare with the constraint of a vanishing pressure gradient $\int_0^L \partial_x p dx = 0$). It is therefore hoped that the present work will stimulate new experiments and modeling efforts aiming at a better knowledge of the dynamics of nonlinear nonlocal waves.

ACKNOWLEDGMENT

I thank F. H. Busse for fruitful comments.

APPENDIX: FOURIER-GALERKIN SCHEME

1. Generalities

Only pure Fourier modes, in $\exp(ikx)$, of the velocity and temperature fields are considered; thus fields depending only on $y \in [0, \Gamma]$ and $z \in [-1/2, 1/2]$ are to be expanded on Galerkin base functions. In order to allow for a tunable value of Γ , the flow domain is mapped to $[-1, 1]^2$ through the change of coordinates

$$Y = (2y - \Gamma)/\Gamma, \quad Z = 2z. \quad (\text{A1})$$

For the velocity components of a modulated mode $k \neq 0$ [see Eq. (6)], one must write

$$v_{ky} = \sum_n \sum_m \tilde{v}_{ynm} B_n^y(Y) A_m^z(Z), \quad (\text{A2a})$$

$$v_{kz} = \sum_n \sum_m \tilde{v}_{znm} A_n^y(Y) B_m^z(Z), \quad (\text{A2b})$$

with

$$A_n^r(\pm 1) = B_n^r(\pm 1) = (B_n^r)'(\pm 1) = 0 \quad (\text{A3})$$

for $r = y, z$ in order to satisfy boundary conditions (10) concerning v_{ky} and v_{kz} . For the homogeneous mode of velocity [see Eq. (6)],

$$v_0 = \sum_n \sum_m \tilde{v}_{nm} A_n^y(Y) A_m^z(Z), \quad (\text{A4a})$$

$$\psi_0 = \sum_n \sum_m \tilde{\psi}_{nm} B_n^y(Y) B_m^z(Z) \quad (\text{A4b})$$

fulfill boundary conditions (10) concerning v_0 and ψ_0 . A Fourier mode of the temperature field assumes the form

$$\theta = \sum_n \sum_m \tilde{\theta}_{nm} A_n^y(Y) A_m^z(Z) \quad (\text{A5})$$

for model CC with boundary conditions (11) and (12). For model II, according to boundary conditions (11) and (13), the more complicated ansatz

$$\theta = \sum_m \tilde{\theta}_{0m} A_m^z(Z) + \sum_n \sum_m \tilde{\theta}_{nm} C_n^y(Y) A_m^z(Z) \quad (\text{A6})$$

is necessary, with

$$(C_n^y)'(\pm 1) = \int_{-1}^1 C_n^y(Y) dY = 0. \quad (\text{A7})$$

Model CI, according to boundary conditions (11) and (14), permits the simpler ansatz

$$\theta = \sum_n \sum_m \tilde{\theta}_{nm} D_n^y(Y) A_m^z(Z) \quad (\text{A8})$$

with

$$(D_n^y)'(-1) = D_n^y(1) = 0. \quad (\text{A9})$$

The sums over the integer indices n and m run for

$$n^2 + (m+2)^2 \leq N^2 \quad (\text{A10})$$

with N being the truncation parameter of the Galerkin code; this slightly unsymmetric truncation scheme favors a better resolution in the y direction aiming at the study of the large-gap limit. In order to accelerate the convergence of the scheme in this same limit, it has proven useful to use different scalar products in the Y and Z directions. The scalar product in the Y direction is simply

$$\langle f(Y), g(Y) \rangle_y = \int_{-1}^1 f(Y) g^*(Y) dY; \quad (\text{A11})$$

in the Z direction, in order to favor a better resolution of the corresponding boundary layers,

$$\langle f(Z), g(Z) \rangle_z = \int_{-1}^1 f(Z) g^*(Z) dZ / \sqrt{1-Z^2} \quad (\text{A12})$$

is preferred. The polynomials A_n^y , B_n^y , C_n^y , D_n^y are constructed with the Gram-Schmidt orthogonalization scheme from simple polynomials fulfilling the corresponding boundary conditions, the scalar product being given by Eq. (A11). The same procedure is used to construct the polynomials A_m^z and B_m^z with the scalar product (A12). Special care is taken to insure the symmetry properties

$$\begin{aligned} A_m^z(-Z) &= (-1)^{m+1} A_m^z(Z), \\ B_m^z(-Z) &= (-1)^{m+1} B_m^z(Z). \end{aligned} \quad (\text{A13})$$

Thus the active even modes fulfilling Eq. (16) correspond to Eq. (A2a) with m odd, Eq. (A2b) with m even, Eqs. (A5), (A6) or (A8) with m even; the passive homogeneous mode correspond to Eq. (A4a) with m even, Eq. (A4b) with m odd, Eqs. (A5), (A6) or (A8) with m odd; the passive ‘‘modulated modes’’ correspond to Eq. (A2a) with m even, Eq. (A2b) with m odd, Eqs. (A5), (A6) or (A8) with m odd. The equations for v_{ky} and v_{kz} are the y and z components of vorticity equation (7); these components imply the x component of the

vorticity equation, since this equation in a curl and x -Fourier modes are considered. With the method of the weighted residuals, $(7) \cdot \hat{\mathbf{y}}$ and $(7) \cdot \hat{\mathbf{z}}$ give ordinary differential equations (ODEs) for the coefficients \tilde{v}_{ynm} and \tilde{v}_{znm} , the bidimensional scalar product being naturally given by the combination of Eqs. (A11) and (A12), i.e.,

$$\begin{aligned} & \langle f_1(Y)f_2(Z), g_1(Y)g_2(Z) \rangle \\ &= \langle f_1(Y), g_1(Y) \rangle_y \langle f_2(Z), g_2(Z) \rangle_z. \quad (\text{A14}) \end{aligned}$$

The same method is used to derive from heat equation (5) the ODEs for the coefficients $\tilde{\theta}_{nm}$. Finally, the ODEs for the coefficients \tilde{v}_{nm} and $\tilde{\psi}_{nm}$ are obtained from Eqs. (8) and (7) $\cdot \hat{\mathbf{z}}$. Naturally even and odd modes are treated separately; the adjoint linear problem for even modes, needed to compute the adjoint critical mode U_1^c [see Eq. (36)], is deduced from the consideration of the adjoints of the corresponding linear matrices. Full matrices are obtained, but the convergence of the code is rather fast. For instance, the computations of the

critical data displayed in Figs. 2 and 3 are achieved with $N=18$ for $\eta \leq 1000$, whereas $N=20$ is sufficient to obtain converged results for $\eta=1500$. The limitation of the code concerns the nonlinear terms, which yield quite large and full tables of coefficients.

2. Computation of the global mode

The computations of the large-scale mode V_2^l from Eq. (26), and hence of the global mode V_2^g from $V_2^h - V_2^l$ are very demanding and slowly converging. The following scheme has therefore been employed to accelerate the convergence of these computations. The form V_0^g of the global mode is first computed by a direct solution of the linear problem (33) assuming $M=1$. Spatial averages of the ratios between the fields in $V_2^g = V_2^h - V_2^l$ and the same fields in V_0^g then yield the (approximate) value of M . For subsequent computations $V_2^g = MV_0^g$ is used instead of the first estimate $V_2^g = V_2^h - V_2^l$, because this yields much smoother fields.

-
- [1] M.C. Cross and P.C. Hohenberg, *Rev. Mod. Phys.* **65**, 851 (1993).
- [2] H. Chaté, *Nonlinearity* **7**, 185 (1994).
- [3] T. Leweke and M. Provansal, *Phys. Rev. Lett.* **72**, 3174 (1994).
- [4] I.S. Aranson and L. Kramer, *Rev. Mod. Phys.* **74**, 99 (2002).
- [5] L. Ning and R.E. Ecke, *Phys. Rev. E* **47**, 3326 (1993).
- [6] H.F. Goldstein, E. Knobloch, I. Mercader, and M. Net, *J. Fluid Mech.* **248**, 583 (1993).
- [7] Y. Liu and R.E. Ecke, *Phys. Rev. Lett.* **78**, 4391 (1997).
- [8] Y. Liu and R.E. Ecke, *Phys. Rev. E* **59**, 4091 (1999).
- [9] E.Y. Kuo and M.C. Cross, *Phys. Rev. E* **47**, R2245 (1993).
- [10] J. Herrmann and F.H. Busse, *J. Fluid Mech.* **255**, 183 (1993).
- [11] M.V. Hecke and W.V. Saarloos, *Phys. Rev. E* **55**, R1259 (1997).
- [12] In the context of instabilities leading to *stationary* patterns, i.e., of envelope equations with *real* coefficients, Ref. [13] has established the existence of similar nonlocal effects in the Taylor-Couette system. This model has been extended phenomenologically to explain some relevant features of spiral turbulence in Ref. [14].
- [13] P. Hall, *Phys. Rev. A* **29**, 2921 (1984).
- [14] F. Hayot and Y. Pomeau, *Phys. Rev. E* **50**, 2019 (1994).
- [15] E. Plaut and F.H. Busse, *J. Fluid Mech.* **464**, 345 (2002).
- [16] P.G. Daniels and C.F. Ong, *J. Fluid Mech.* **215**, 503 (1990).
- [17] H. Riecke and L. Kramer, *Physica D* **137**, 124 (2000).
- [18] T. Clune and E. Knobloch, *Phys. Rev. E* **47**, 2536 (1993).
- [19] M.V. Hecke, Ph.D. thesis, Universiteit Leiden, 1996.
- [20] H.F. Goldstein, E. Knobloch, I. Mercader, and M. Net, *J. Fluid Mech.* **262**, 293 (1994).
- [21] G. Dangelmayr and L. Kramer, in *Evolution of Spontaneous Structures in Dissipative Continuous Systems*, edited by F.H. Busse and S.C. Müller, Lecture Notes in Physics, Vol. m55 (Springer-Verlag, Berlin, 1998), pp. 1–85.
- [22] Q. Feng, W. Pesch, and L. Kramer, *Phys. Rev. A* **45**, 7242 (1992).
- [23] B. Bruhn, B.P. Koch, and P. Jonas, *Phys. Rev. E* **58**, 3793 (1998).
- [24] The *Handbook of Chemistry and Physics*, edited by D.R. Lide (CRC Press, Boca Raton, 2001), indicates that for water at 25 °C, $\kappa = 1.5 \times 10^{-7}$ m²/s, $P = 6.3$; for mercury at 25 °C, $\kappa = 4.4 \times 10^{-6}$ m²/s, $P = 0.0257$. The values for argon at 23 °C, $p = 30$ bars, $\kappa = 6.8 \times 10^{-7}$ m²/s, $P = 0.69$, are taken from J. Liu and G. Ahlers, *Phys. Rev. Lett.* **77**, 3126 (1996).
- [25] P. Kolodner, *Phys. Rev. Lett.* **66**, 1165 (1991).
- [26] J. Niemela, G. Ahlers, and D.S. Cannell, *Phys. Rev. Lett.* **64**, 1365 (1990).
- [27] J. Lega, B. Janiaud, S. Jucquois, and V. Croquette, *Phys. Rev. A* **45**, 5596 (1992).
- [28] B. Janiaud, A. Pumir, D. Bensimon, V. Croquette, H. Richter, and L. Kramer, *Physica D* **55**, 269 (1992).